Article

Intercomparison of Automated Near-Real-Time Flood Mapping Algorithms Using Satellite Data and DEM-Based Methods: A Case Study of 2022 Madagascar Flood

Wenzhao Li , **Dongfeng Li and Zheng N. Fang ***

Department of Civil Engineering, The University of Texas at Arlington, Arlington, TX 76019, USA
* Correspondence: nickfang@uta.edu

Abstract: Numerous algorithms have been developed to automate the process of delineating water surface maps for flood monitoring and mitigation purposes by using multiple sources such as satellite sensors and digital elevation model (DEM) data. To better understand the causes of inaccurate mapping information, we aim to demonstrate the advantages and limitations of these algorithms through a case study of the 2022 Madagascar flooding event. The HYDRAFloods toolbox was used to perform preprocessing, image correction, and automated flood water detection based on the state-of-the-art Edge Otsu, Bmax Otsu, and Fuzzy Otsu algorithms for the satellite images; the FwDET tool was deployed upon the cloud computing platform (Google Earth Engine) for rapid estimation of flood area/depth using the digital elevation model (DEM) data. Generated surface water maps from the respective techniques were evaluated qualitatively against each other and compared with a reference map produced by the European Union Copernicus Emergency Management Service (CEMS). The DEM-based maps show generally overestimated flood extents. The satellite-based maps show that Edge Otsu and Bmax Otsu methods are more likely to generate consistent results than those from Fuzzy Otsu. While the synthetic-aperture radar (SAR) data are typically favorable over the optical image under undesired weather conditions, maps generated based on SAR data tend to underestimate the flood extent as compared with reference maps. This study also suggests the newly launched Landsat-9 serves as an essential supplement to the rapid delineation of flood extents.

Keywords: near-real-time flood mapping; Landsat-9; Sentinel; mNDWI; HYDRAFloods; Otsu thresholding algorithms; FwDET; Google Earth Engine; urban flood inundation

1. Introduction

Many countries worldwide have experienced significant economic and infrastructure damage and loss of lives from flooding [1], especially for those with limited resources [2]. Rapid water mapping for flooding is essential for managing first responders' operations and implementing best management practices after disasters [3]. To allocate relief efforts and organize preventative measures against flood damage, emergency responders also need timely and accurate information on the areas affected by floodwater [4]. Remotely sensed data by satellites and aircraft have been applied in flood monitoring/delineating and other water resource management [5]. It is an approachable and critical method for developing countries to utilize with rapidly gathered information so that detailed snapshots of floods can be provided [6,7].

Remote sensing data can help with flood monitoring and management, ranging across a variety of fields, such as flood risk and damage assessment [8,9], surface water detection [10,11], water level monitoring [7,12], flood model calibration and validation [13,14], data assimilation [15,16], and remote sensing-derived floodplain topography [17,18]. Revilla-Romero et al. [11] showed the use of a multiyear surface water product from Moderate Resolution Imaging Spectroradiometer (MODIS) satellite imagery to improve global

flood forecasting. Horritt [13] used satellite-borne synthetic-aperture radar imagery as calibration and validation data for a two-dimensional finite element flood flow model. Massari et al. [15] assimilated Advanced SCATterometer (ASCAT) soil moisture products to improve the simulations of a rainfall-runoff model. Fassoni-Andrade [17] presented a high-resolution topographic mapping (30 m) of the middle-lower Amazon floodplain using Landsat imagery.

Meanwhile, efforts have also been made to improve the algorithms for automated surface water mapping using remote sensing data. These algorithms include (1) thresholding of single bands and spectral indexes [19,20], (2) knowledge-based water detection from other land cover types based on the spectral properties [21,22], spectral mixture analysis (SMA) [23,24], and machine learning methods including both supervised and unsupervised classification schemes [25,26]. DeVries et al. [27] applied a fully automated and scalable algorithm that estimated the subpixel water fraction using Landsat data over large areas. Huang et al. [28] presented an automated surface water extraction algorithm using Sentinel-1 synthetic-aperture radar (SAR) imagery. Kordelas et al. [29] applied an unsupervised approach based on the automatically selected threshold on the shortwave infrared (SWIR) band to better distinguish between different types of flooded wetlands using Sentinel-2 optical images. Cao et al. [30] developed an automated algorithm to find the image segmentation threshold for operational flood mapping using Sentinel-1 SAR Imagery. Donchyts et al. [31] created a similar segmentation algorithm that extracts water edges for threshold sampling. Bo et al. [3] utilized a self-supervised machine learning framework for patch-wise urban flood mapping using bitemporal multispectral satellite imagery. Acharya et al. [26] evaluated multiple machine learning algorithms such as naive Bayes (NB), support vector machines (SVM), and random forest (RF) to extract surface water in Nepal. Bazi et al. [32] presented an SAR-based automatic approach to assess the water surface changes in Saskatchewan, Canada, where the expectation maximization (EM) algorithm [33] was applied to obtain maximum likelihood estimates of the mixture parameters. Among the water mapping algorithms, the thresholding-based methods have been most widely used since they are computationally less time-consuming and could produce accurate results compared to other approaches of higher complexity [34–38].

In addition, automated and rapid flood inundation modeling using a digital elevation model (DEM) can supplement the necessary flood information when real-time satellite images are unavailable, as shown in the latest studies [18,39,40]. The applications above using multiple data sources with automated flood mapping are highly beneficial and desirable for a time-sensitive disaster situation in flood response practices.

However, rapid-deployed and reliable flood mapping based on satellite or DEM data during extreme events is still very challenging due to uncertainties and limitations of the high-quality remote sensing data, the methods, and the high demand for computational resources. Advances in cloud-based data providers and computational platforms such as Google Earth Engine (GEE) [41] provide a way to address computational difficulties and allow state-of-the-art tools to operate seamlessly in any region of interest. Many Earth observation datasets are made easily accessible and analyzable free of charge through GEE. These include the latest Landsat-9 dataset (launched in September 2021 and made available in October 2021), which is designed to replace Landsat-7. The combination of Landsat-8 and Landsat-9 data collection can provide global observation every 8 days.

With the proliferation of the computational power of GEE and the latest free but high-quality satellite data now and forthcoming, there is still an urgent need to understand the new satellite data and water mapping algorithms regarding their strengths and limitations, especially with quick deployment and automation. Therefore, this research aims to (1) investigate the pros and cons of different satellite imagery for water surface mapping with a focus on the SAR and optical images and (2) compare and evaluate the different automated methods for surface water extraction from satellite images and DEM. We achieved these goals by conducting a flood inundation study for a flood event in Madagascar (January 2022). This study allows us to gain insight into the advances in leveraging

remote sensing image analysis and cloud computing for developing countries' flood hazard monitoring and management.

2. Materials and Methods

2.1. Study Area

Madagascar is situated between the latitudes 12° and 25° S and longitudes 43° and 51° E. It has a tropical maritime climate that is conditioned by altitude, proximity to the sea, and monsoons. The mean annual temperature ranges from 23 to 27 °C in coastal areas and from 14 to 22 °C in the highlands. The climate is clearly separated into two seasons: a rainy and hot season from November to April, and a dry and cool season from May to October, with total annual rainfall ranging from 350 mm on the southwest coast to 4000 mm on the east coast. During the rainy season, the eastern and northern coasts receive heavy rainfall brought by tropical cyclones. Meanwhile, thunderstorms are also common in the central highlands in the same season [42,43].

Excessive rainfall caused by two recent (2022) tropical weather systems impacted Madagascar, particularly in the country's capital, Antananarivo, and its surrounding metropolitan regions. The rains were driven by an Intertropical Convergence Zone around the equator on 17 January 2022 and then increased on 22 January 2022 after a cyclone made landfall in the east of the country. The event had driven disastrous hazards of loss of life. According to the United Nations Office for the Coordination of Humanitarian Affairs (OCHA) [44], over 58,000 people were affected across the central Analamanga Region, including 58 lives that were lost. Many houses in the capital area collapsed or were swept away, leaving others underwater or at risk of flooding and landslides. In a developing country such as Madagascar, resources are limited, especially during natural hazards. Figure 1 presents the map of Antananarivo and its surrounding regions, including the local river channel and the only available reference map of flooding and damage grade assessment produced by the EU Copernicus Emergency Management Service—Mapping platform (https://emergency.copernicus.eu/mapping/ems/emergency-management-service-mapping, accessed on 1 February 2022), which is used as the reference map (28 January 2022) for this study.
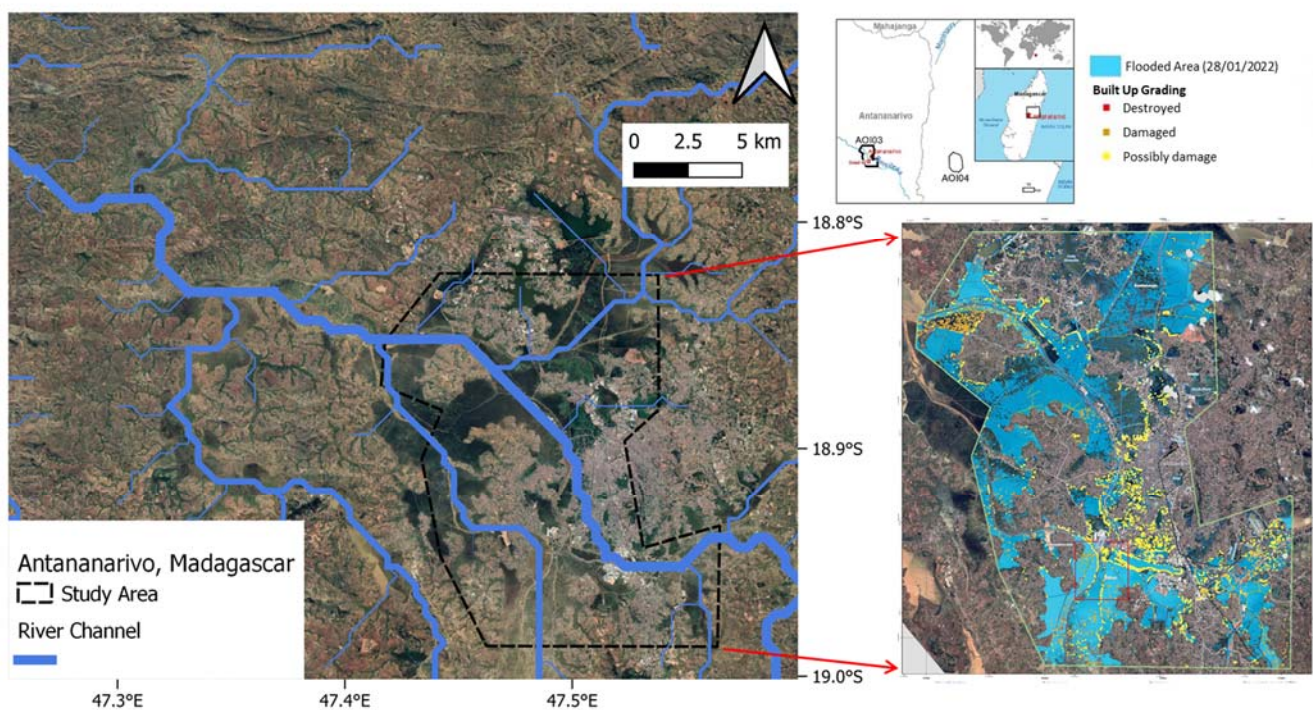

Figure 1. Study area and reference map.

2.2. Data

2.2.1. Precipitation and Satellite Images

The precipitation data used as a reference in this study were obtained from Global Precipitation Measurement (GPM) version 6 dataset [45], which uses the Integrated Multi-satellitE Retrievals for GPM (IMERG) algorithm at a spatial resolution of 0.1° (11 km). The precipitation product from GPM was improved after the calibration process for the study period from December 2021 to early February 2022. According to the rainfall time series as shown in Figure 2, the study period can be divided into two different periods (Figure 2): (1) the first period (22 December 2021–15 January 2022) as the preflooding period and (2) the second period (27 January 2022–2 February 2022) as the after-flooding period, which shows the destructive impacts from the consecutive rainfall events, especially the major event on 17 January to 22 January 2022. For the first period, there is an event (maximum hourly rate > 12 mm/h) on 31 December 2021 that could also induce extensive flooding in the study area.
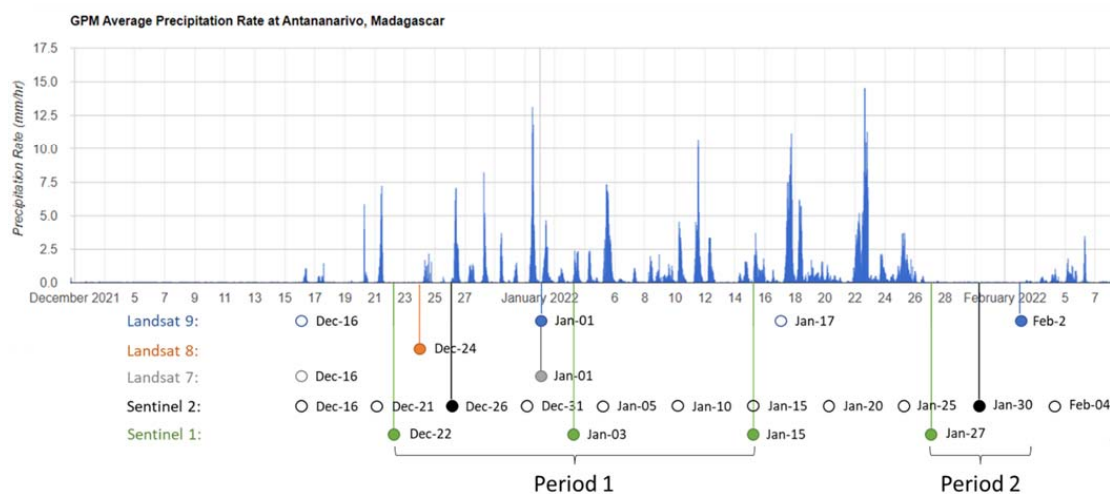

Figure 2. Time series of the rainfall intensity and satellite-available dates (solid dots show the images with lower cloud coverage used in the study) in the study area (rainfall data source: GPM).

This study uses high-resolution products from Landsat-7/8/9 and Sentinel-1 and -2 for spatiotemporal analysis of the surface water areas. All the NASA Landsat-7/8/9 multispectral images provide visible and near-infrared (VNIR), shortwave infrared (SWIR), thermal infrared (TIR), and quality assessment (QA) bands. This study uses the Green and SWIR bands to calculate the modified normalized difference water index (mNDWI) [46] to identify the water surface from the land surface. It is noted that the "strip" issue in Landsat-7 data was not addressed due to higher cloud coverage. All of the mNDWI layer was processed to 30 m spatial resolution. The QA band removes low-quality observations such as clouds, cirrus, and cloud shadow to minimize their impacts on the water surface identification. The 30 m mNDWI was also calculated and processed from the Sentinel-2 images obtained from the European Space Agency (ESA) mission with two twin polar-orbiting satellites as a constellation (Sentinel-2A and Sentinel-2B), with a global 5-day revisit time.

For the synthetic-aperture radar (SAR) images, we used Sentinel-1 ground-range-detected (S1_GRD) images at C-band (central frequency of 5.404 GHz) with a global 6- or 12-day revisit time. Sentinel-1 is a mission of ESA with twin satellites (Sentinel-1A and Sentinel-1B) as a constellation. In this study, we only use the vertical transmit, vertical receive (VV) backscatter data with 10 m spatial resolution, as suggested by [47,48]. These data were preprocessed (e.g., thermal noise removal, radiometric calibration, and terrain correction) with the Sentinel-1 Toolbox and processed to 30 m resolution. The characteristics of the satellite images from Landsat-7/8/9 and Sentinel-1/2 are summarized in Table 1.

Table 1. Characters of the satellite images used in this study.

Satellite	Provider	Sensor	Polarization/Band	Resolution	Wavelength
Sentinel-1	ESA	C-band SAR	VV	10 m	~5.55 cm
Sentinel-2	ESA	Multispectral Instrument (MSI)	Green	10 m	~0.56 μm
			SWIR	20 m	~1.61 μm
Landsat-7	NASA	Enhanced Thematic Mapper Plus (ETM+)	Green	30 m	0.52–0.60 μm
			SWIR	30 m	1.55–1.75 μm
Landsat-8	NASA	Operational Land Imager (OLI)	Green	30 m	0.53–0.59 μm
			SWIR	30 m	1.57–1.65 μm
Landsat-9	NASA	Operational Land Imager 2 (OLI 2)	Green	30 m	0.53–0.59 μm
			SWIR	30 m	1.57–1.65 μm

As shown in Figure 2, a total of 10 satellite images were acquired at the following names and dates, respectively: Sentinel-1 (22 December 2021), Landsat-8 (24 December 2021), Sentinel-2 (26 December 2021), Landsat-9 (1 January 2022), Landsat-7 (1 January 2022), Sentinel-1 (3 January 2022), Sentinel-1 (3 January 2022), Sentinel-1 (15 January 2022), Sentinel-1 (27 January 2022), Sentinel-2 (30 January 2022), and Landsat-9 (2 February 2022).

2.2.2. DEM Data

The elevation information is essential for the surface water detection models to generate logical results that surface water usually accumulates at the lowest relative points within a local drainage system. The elevation data from the digital elevation model (DEM) are also required as the surface water mapping model input. In this research, we use six different DEM or digital surface model (DSM) datasets to compare the associated water surface products, including the (1) Japan Aerospace Exploration Agency (JAXA) Advanced Land Observing Satellite (ALOS) DSM V2.2 product [49], (2) World Wide Fund for Nature (WWF) HydroSHEDS Void-Filled DEM [50], (3) WWF HydroSHEDS Hydrologically Conditioned DEM [50], (4) Multierror Removed Improved-Terrain (MERIT) DEM [51], (5) Global Multiresolution Terrain Elevation Data 2010 (GMTED2010) [52], and (6) NASA/USGS Shuttle Radar Topography Mission (SRTM) V3 product [53]. Figure 3 shows the terrain maps based on the selected DEM datasets. For more details, Table 2 provides additional information on their spatial resolution and references.
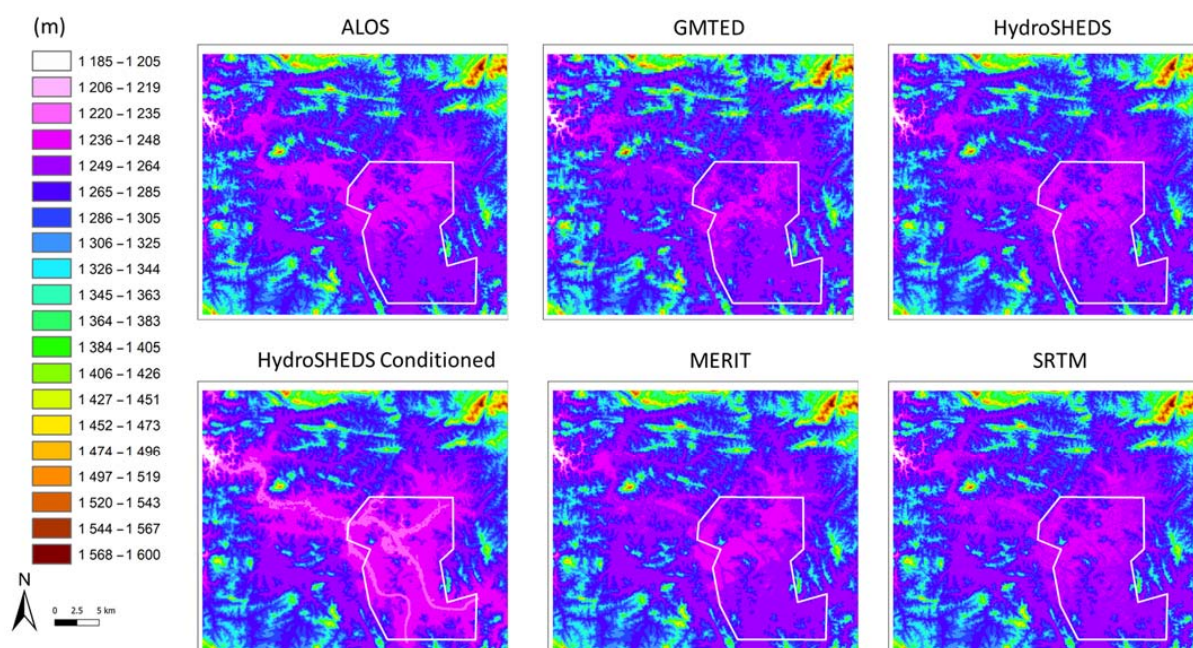

Figure 3. DEM products in the study area.

Table 2. Characters of the DEM data used in this study.

Satellite	Provider	Resolution	Reference
ALOS	JAXA	30 m	[49]
HydroSHEDS	WWF	93 m	[50]
HydroSHEDS Hydrologically Conditioned	WWF	93 m	[50]
MERIT	Dai Yamazaki	93 m	[51]
GMTED 2010	USGS	232 m	[52]
SRTM	NASA/USGS	30 m	[53]

2.3. Automated Satellite-Based Surface Water Mapping

In this research, the satellite-based surface water mapping assessment was performed using the modified toolsets from Hydrologic Remote Sensing Analysis for Floods (HYDRAFloods: https://github.com/Servir-Mekong/hydra-floods/tree/master/hydrafloods, accessed on 1 May 2022). HYDRAFloods is an open source Python framework for obtaining, processing, and generating surface water maps assessed from both optical (e.g., Landsat-7/8/9) and SAR (Sentinel-1) satellite remote sensing images. The framework is developed and deployed on the GEE and Google Cloud Platform (GCP), which provide automated, rapid, and high-quality surface water mapping products to the users with minimal effort. In this study, the data downloading, image processing, water surface detection, data visualization, and analysis were carried out on top of Earth Engine Python API. The results were computed in GCP and evaluated in the GEE integrative interface. Figure 4 outlines the workflow of the water surface detection using HYDRAFloods, where details of image preprocessing and water mapping algorithms are introduced in the following sections.
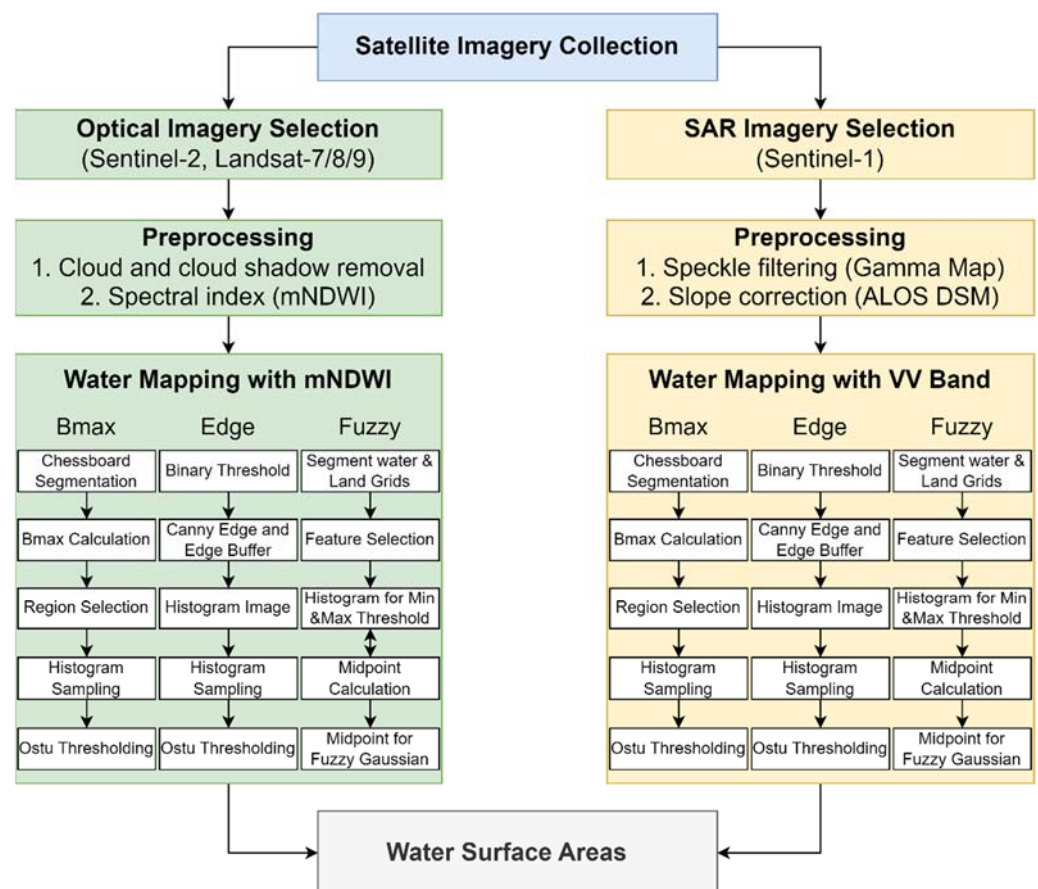
Figure 4. The workflow of automated satellite-based surface water mapping.

2.3.1. Image Preprocessing

Image preprocessing is usually required for the raw satellite images to correct the atmospheric and terrain effects for practical applications. For the optical images, we used the quality assurance bits in "QA" generated using the C function of mask (CFMask) [54] algorithm to remove the pixels that are affected by snow/ice, cirrus, cloud, and cloud shadow. The processed images are used to generate mNDWI products based on the Green and SWIR bands. The mNDWI is calculated using the equation [46]:

$$mNDWI = (Green - SWIR)/(Green + SWIR), \tag{1}$$

For SAR images, since the data collection on the GEE was already preprocessed, we will focus on the algorithms for SAR speckle filtering and slope correction, respectively. Speckle appears in SAR images like granular noise that is caused by the interference of radar waves reflected from the elementary scatterers on the ground. Because speckle typically lowers the accuracy of image segmentation and classification in SAR images, adding speckle filters is a standard preprocessing step to alleviate the effects of speckle. The scientific community has developed multiple algorithms (e.g., Lee Sigma [55], Gamma Map [56], and Refined Lee [57]) which are also incorporated into HYDRAFloods toolsets. In this study, we used the Gamma Map algorithm, as suggested by the tool.

Meanwhile, the SAR images are also sensitive to the terrain effects. In this study, we applied an angular-based radiometric slope correction routine using ALOS data to reduce the impact of terrain on the SAR data. More details regarding the algorithm and the input arguments can be found in Vollrath et al. [58].

2.3.2. Mapping Algorithm

There are multiple surface water mapping algorithms provided in the HYDRAFloods toolsets. Many algorithms are developed as variations of Otsu's method [59], a classical method that uses the maximum between-class histogram variance as the criterion to determine the threshold value for segmentation. However, this Otsu's method only performs well when the image is characterized by a bimodal histogram, but it is not applicable to images with a unimodal histogram. In this study, we apply three Otsu's variation algorithms and compare the results: (1) Edge Otsu [31,48], (2) Bmax Otsu [30,48], and (3) Fuzzy Otsu [60]. These algorithms provide generic and sensor-agnostic water mapping, given some customization of parameters. More detailed information is introduced in the following sections.

- Bmax Otsu

The Bmax Otsu algorithm was developed by Cao et al. [30] to extract a near-bimodal histogram from the optical or SAR imagery. The major steps are presented in Figure 4. Firstly, the algorithm uses chessboard segmentation to subset the image into grids. Secondly, the maximum value of normalized between-class variance (BCV), or Bmax value, is calculated. The initial threshold value needed to start Bmax calculation is set to −16 dB for Sentinel-1 and 0 for mNDWI of optical imagery (Sentinel-2 and Landsat-7/8/9). Thirdly, the Bmax value is used to select the region of the bimodal feature for histogram sampling. Fourthly, histogram sampling is conducted to generate the distribution of frequency of occurrence of mNDWI or VV backscatter within a specified range. Finally, the segmentation threshold value is computed using Otsu's method. The final surface water map is created where areas with dB values less than the threshold are identified as water for SAR data, and values greater than the threshold are nonwater. In contrast, the threshold value is used inversely, where mNDWI values greater than the threshold value are classified as water for optical data, and those that are smaller than the threshold are nonwater.

- Edge Otsu

The Edge Otsu algorithm was initially introduced by Donchyts et al. [31]. The first step is to generate a binary image from an initial segmentation threshold in order to alleviate any

edges being defined from other classes in the later step. The second step is to use the Canny edge filter [61] to extract the edges of features in the satellite imagery with the assumption that the edges are water. Some defined edges are filtered by length to remove the impacts of small edges that skew the histogram sampling. The algorithm then buffers the delineated edges and generates the image for histogram sampling. The following steps are the same as the Bmax Otsu, which uses Otsu's method to compute the threshold value applied to the entire image to differentiate water and nonwater surfaces. The initial threshold value is also needed and set to −16 dB for SAR and 0 for mNDWI, respectively.

- Fuzzy Otsu

The Fuzzy Otsu method [60] modified the Otsu method based on the mathematics of fuzzy sets by using both the between-class variance and the membership grade from the Fuzzy Gaussian function to improve the segmentation performance. The Fuzzy Gaussian function transforms the pixel values into a normal distribution, where the midpoint of the normal distribution defines the ideal definition for the set, assigning the membership grade to 1, with the remaining input values decreasing as they move away from the midpoint in both the positive and negative directions until the values move too far to remain in the fuzzy set and are therefore assigned zeros [62]. The steps of implementing Fuzzy Otsu include (1) segmenting the pixels of water and lands using the initial threshold value; (2) randomly selecting features to calculate the minimum threshold value using Otsu's method; (3) filtering the image based on the minimum threshold value and calculating the maximum threshold values; (4) calculating the midpoint (arithmetic mean) value of the minimum and maximum threshold values; and (5) inputting the midpoint into the Fuzzy Gaussian function to map water. Unlike the binary image results from Bmax Otsu's and Edge Otsu, the Fuzzy Otsu exported the image decimal values estimated from Gaussian distribution. A parameter ("spread") was set to 0.2 to define the shape of the Gaussian curve. An additional process was included in determining the surface water areas using a cutoff value based on the empirical judgment that pixel values equal to or greater than 0.999 are classified as water, and values less than 0.999 are nonwater.

2.4. Automated DEM-Based Surface Water Mapping

As an available tool for rapid surface water mapping, the DEM-based methods can provide the areal extent of water surface during or after the flood event, which can be validated by satellite images, and the rough floodwater depth that both are essential information for the first responders and mitigation assessment. Here, we used a new cloud-based GIS tool using the DEM information, the Floodwater Depth Estimation Tool (FwDET) [40,63,64], for estimating floodwater extent and depth based solely on a DEM and a flood inundation map (if available). FwDET allows for fast floodwater depth estimation given by the flood extent, and here, we used the study area as the flood extent. The DEM data include ALOS, GMTED, HydroSHEDS, HydroSHEDS conditioned, MERIT, and SRTM. More details of the steps to generate the FwDET water depth and inundation map can be found in [40,64].

3. Results and Discussion

3.1. Satellite-Based Surface Water Mapping Results

The surface water mapping results from each selected satellite imagery are shown in Figure 5a,b during the study period. The first rows of Figure 5a,b show the cloud-masked optical RGB images from Landsat-7/8/9 and original Sentinel-1 SAR greyscale images based on the VV band. The second rows show the mNDWI maps processed from the cloud-masked optical bands from Landsat-7/8/9, as well as the greyscale images from Sentinel-1 VV band preprocessed by speckle filtering and slope correction algorithms. The third to fifth rows show the final surface water maps derived from the second rows using the detection algorithms of Bmax Otsu, Edge Otsu, and Fuzzy Otsu, respectively.
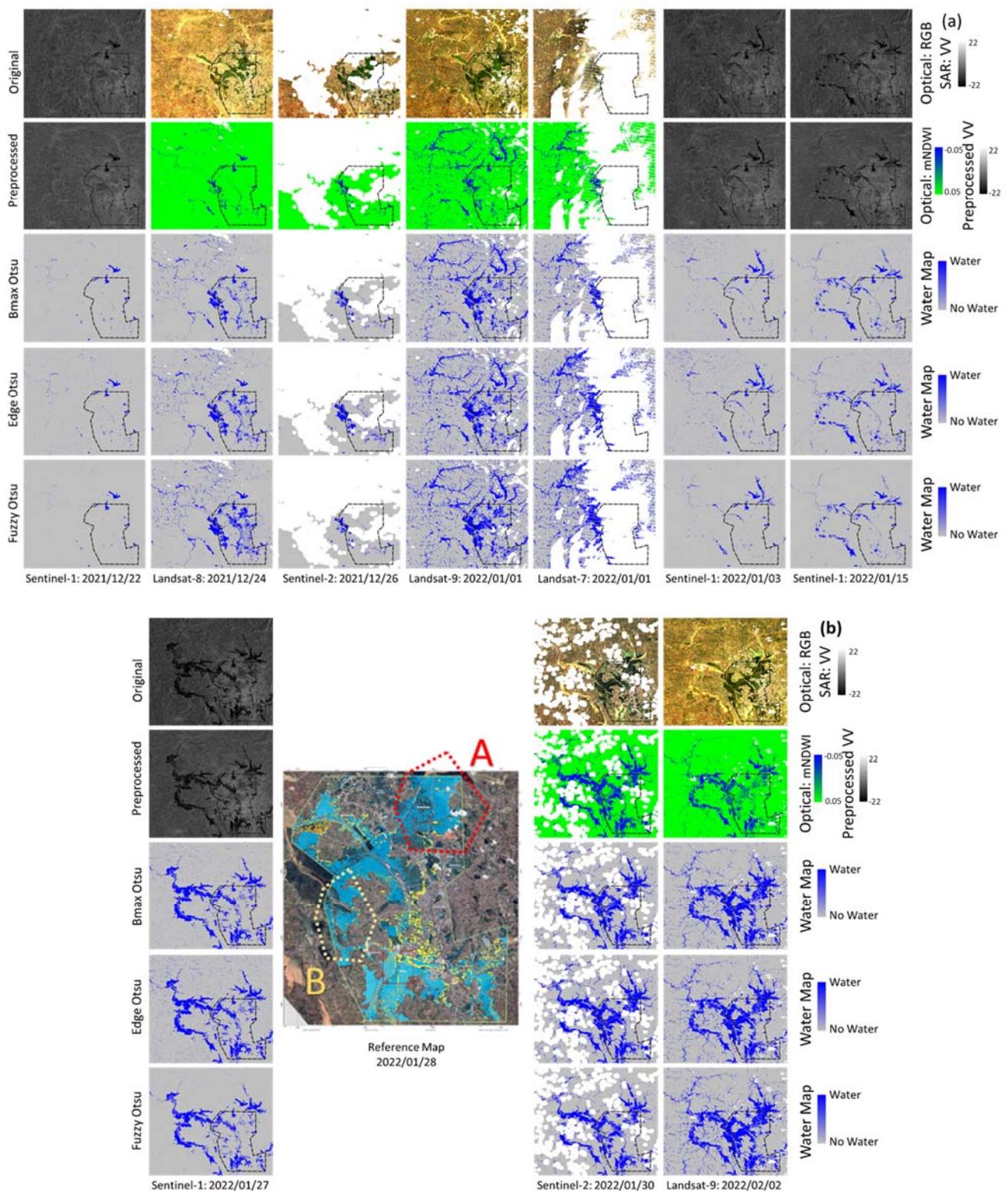
Figure 5. The satellite optical and SAR images, preprocessed VV and mNDWI images, and surface mapping in the study area for the period of (**a**) before the flooding event (22 December 2021–15 January 2022) and (**b**) after the flooding event (27 January 2022–2 February 2022). The flood reference map of 28 January 2022 is included in (**b**), with flooded areas indicated by A and B.

For the first period (22 December 2021–15 January 2022) shown in Figure 5a, the Sentinel-1 image (22 December 2021) shows a limited surface water area, while the Landsat-

8 image (24 December 2021) indicates much more areas than the Sentinel-1, even though no rainfall occurred during the intermediate period. Sentinel-2 image (26 December 2021) shows similar coverage at the boundary of the study area to Landsat-8. However, it only presents limited areas due to cloud contamination. After several rainfall events occurred from 26 December 2021 to 1 January 2022, the Landsat-9 image (1 January 2022) presents additional water surface areas, especially in the northern region, where the Landsat-7 image at the same date also shows similar water surface areas if not covered by the clouds. Compared with Landsat-7 and -9 images on 1 January 2022, the Sentinel-1 image of 3 January 2022 still shows limited surface water area. Sentinel-1 (15 January 2022) shows more surface water in the western region due to the consecutive rainfalls between 3 January 2022 and 15 January 2022.

For the second period (27 January 2022–2 February 2022) shown in Figure 5b, more areas are identified as water surfaces, such as the map from Sentinel-1 on 27 January 2022. However, Sentinel-1 shows many fewer flooded areas in Regions A and B, marked by the reference map, indicating that the results from Sentinel-1 (27 January 2022) underestimate the flood area. Meanwhile, Sentinel-2 (30 January 2022) and Landsat-9 (2 February 2022) show a similar flooded area in term of its coverage in Regions A and B. Landsat-9 provides a more comprehensive perspective than Sentinel-2 with less cloud coverage.

Additionally, the histogram of the sampling and the identified threshold values are presented in Figure 6. While some of the satellite images (e.g., Landsat-9 on 1 January 2022) show similar distributions in the histograms among different algorithms, most of the histograms are dissimilar, resulting in different threshold values. The results from Figures 5 and 6 are summarized in Table 3. It is noted that the midpoint threshold values by the Fuzzy Otsu algorithm are calculated as the arithmetic mean of the "Max" and "Min" values. Additional information on the threshold values for each Otsu algorithm is also included. Among the Otsu algorithms for the same dates, the SAR image (i.e., Sentinel-1) shows a pattern of Edge > Bmax > Fuzzy for both water surface area and threshold values, while for the optical image (e.g., Landsat-7, -8, and -9), a pattern Fuzzy > Bmax > Edge is shown regarding the threshold values, and Fuzzy > Edge > Bmax is shown concerning the water areas. For the Sentinel-2 images affected by the cloud contamination, the Fuzzy surface areas are found to be less than those from Edge and Bmax algorithms. For the same algorithm among different dates, the threshold also varies based on the inundation areas: (1) SAR Sentinel-1 images show the lowest threshold values in no flood (22 December 2021, 3 January 2022), lower values in less flooded (15 January 2022), and highest value in most flooded (27 January 2022) conditions; and (2) optical images from Landsat-7/8/9 and Sentinel-2 images also show higher threshold values in flooded condition than less flooded conditions.

Table 3. The values of threshold values and areas (km^2) of each algorithm from the satellite observations.

| Date	Satellite	Bmax Otsu		Edge Otsu		Fuzzy Otsu	
		Threshold	Area (km^2)	Threshold	Area (km^2)	Threshold	Area (km^2)
22 December 2021	Sentinel-1	−14.7248	4.03	−13.9537	4.69	−17.3227	2.74
24 December 2021	Landsat-8	−0.0782	22.1	−0.0981	31.71	−0.0435	40.92
26 December 2021	Sentinel-2 *	−0.0837	6.53	−0.188	13.65	0.0211	5.26
1 January 2022	Landsat-9	−0.054	40.76	−0.062	46.47	−0.0035	55.23
1 January 2022	Landsat-7 *	−0.0419	5.26	−0.074	6.72	−0.00655	6.85
3 January 2022	Sentinel-1	−14.7336	6.26	−13.9492	7.51	−16.41695	4.56
15 January 2022	Sentinel-1	−14.2097	11.05	−13.4397	13.27	−15.77585	7.85
27 January 2022	Sentinel-1	−13.6915	40.07	−13.1814	42.69	−15.39185	32.54
30 January 2022	Sentinel-2 *	−0.028	63.08	−0.0599	69.88	0.087	52.79
2 February 2022	Landsat-9	−0.058	73.41	−0.062	75.3	−0.0015	80.21

* Images with cloud coverage.
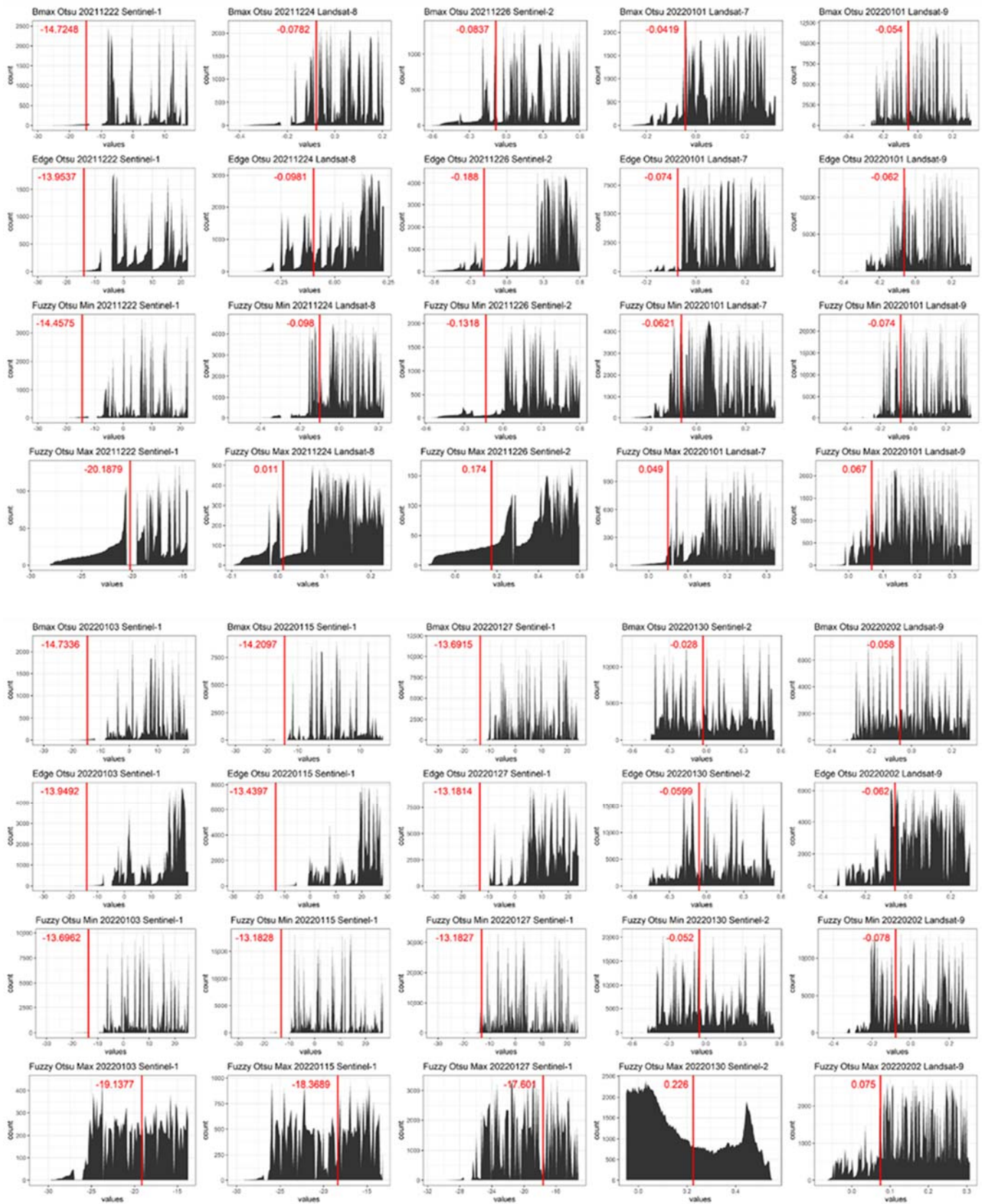
Figure 6. The histograms and the threshold values identified by each algorithm for the satellite imagery.

3.2. DEM-Based Surface Water Mapping Results

The surface water maps that are based on the FwDET-GEE algorithm from each DEM product (ALOS, GMTED 2010, HydroSHEDS, HydroSHEDS Hydrologically Conditioned, MERIT, and SRTM) and the reference map are presented in Figure 7. Overall, the DEM products show a general consistency with the reference map concerning the water surface areas, while some local regions in the north (marked by A), middle east (marked by B), and south (marked by C) indicate an overestimation of the water surface areas, yet middle west regions (marked by region D) in GMTED, MERIT, and SRTM flood products underestimate the flooded area. The spatial resolution acts as a key role in affecting the DEM-based products, as indicated by the similar results from identical spatial resolution (e.g., 30 m from ALOS and SRTM) products. Meanwhile, the products in the same spatial resolution can also produce different results, such as the differences found among 90 m HydroSHEDS, HydroSHEDS conditioned, and MERIT flood products.
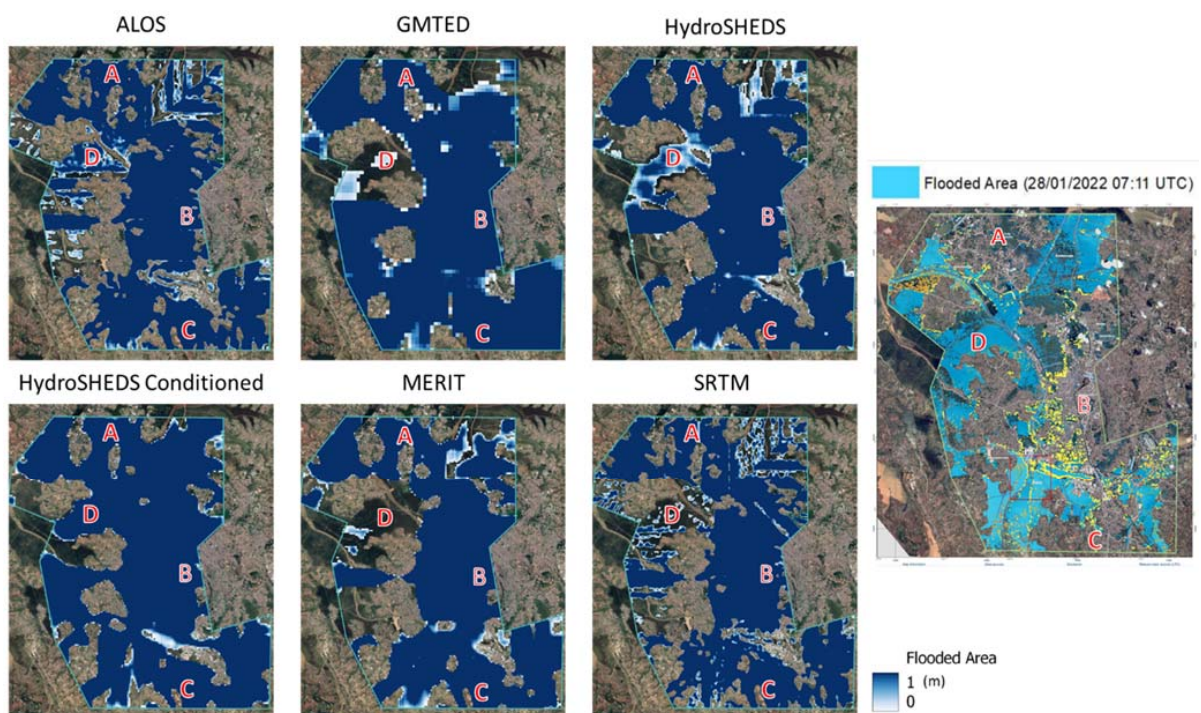

Figure 7. Flood water surface maps based on the FwDET-GEE algorithm from multiple DEM sources (ALOS, GMTED, HydroSHEDS, HydroSHEDS conditioned, MERIT, and SRTM), with flood reference map included, with flooded areas indicated by A, B, C and D.

Figure 8 further illustrates the ALOS DEM and its elevation differences from other DEM datasets. The red regions show an elevation lower than ALOS, and the blue regions are higher. The extensive red areas in HydroSHEDS conditioned map indicate that many regions are lower than ALOS DEM and, therefore, explains more flooded area than those retrieved from ALOS data. The DEM data also show that high slope regions marked by A and C drain the water faster and will not accumulate the water inundation as much as the model predicted. However, the local elevation values may not fully explain the results without considering their relative differences from surrounding areas, such that the region marked by D in MERIT has a lower elevation than that in ALOS, yet it shows no inundation compared with results from ALOS and other datasets, which may be due to its relatively higher elevation than the western area near the flood boundary.
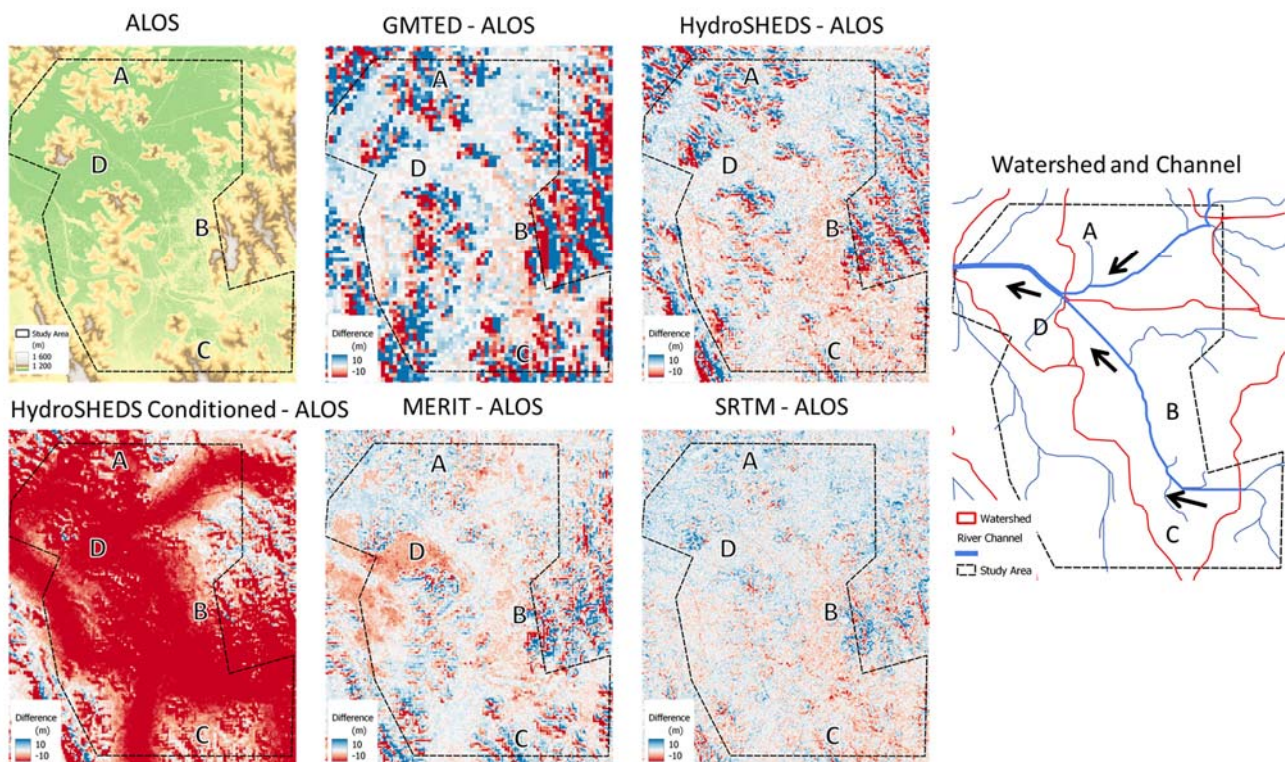
Figure 8. ALOS DEM, its differences with other DEM datasets, and the study area's watershed and channel flow map.

4. Discussion

The results in Figure 3 and Table 3 indicate that Bmax Otsu and Edge Otsu generally produce similar results compared to those from Fuzzy Otsu. Even though the sampling processes to create the histogram are different, the threshold values from Bmax Otsu and Edge Otsu are nearly identical, especially in the cases of using Sentinel-1 SAR images, which is an indicator of the reliability of the threshold values. On the other hand, Fuzzy Otsu seems to be a more robust approach that allows the output to be nonbinary. While the Bmax Otsu and Edge Otsu show more water areas in the SAR imagery, the Fuzzy Otsu can detect more water areas in the optical sensors from Landsat-8/9. Between Bmax and Edge results, the flood inundation is slightly wider based on the Edge Otsu algorithm. More tuning efforts are needed to find the proper parameters and settings (e.g., spread value) to identify water pixels effectively. It is also noted that while the threshold values are estimated based on the entire image area, the result is evaluated only in part of the region (right corner). For some optical images that are heavily affected by cloud contaminations (Sentinel-2 and Landsat-7 images in this case), this will result in a limited area that is available for histogram sampling and will eventually change the threshold values. Therefore, it is critical to conclude that image quality is important for water mapping algorithms.

In this study, Sentinel-1 delivers SAR images reliably every 12 days, which is invaluable for monitoring floods, especially considering the restrictions imposed by unfavorable weather conditions on the optical sensors; however, if an optical image of flooding can be acquired, obtaining useful information from this is straightforward and easier. In addition, the intercomparison of the SAR and optical sensors shows that the surface water areas identified from the SAR images (Sentinel-1) are more likely less than those retrieved from optical images. This may result from the images' features, such as the band or band-derived indexes (VV or mNDWI), image preprocessing and correction, and automated algorithms used in HYDRAFloods. The newly available Landsat-9 data demonstrate the capability of effectively delineating flood-impacted areas, especially when the other optical images (Sentinel-2 and Landsat-7) were hindered by cloud contamination. Landsat-9 data will

continue playing a critical role in adding timely information for flood monitoring, as the recently retired Landsat-7 mission has subsided. It is noted that the differences in wavelength ranges of Green and SWIR bands among Landsat-7, Landsat-8/9, and Sentinel-2 may also marginally change mNDWI values that impact the threshold for water surface mapping. Furthermore, high-resolution commercial images (e.g., Worldview, Pleiades, Planet optical imagery, and Capella and ICEYE SAR imagery) will provide more precise information when incorporated into the algorithms. Still, the increased pixel density brings in requirements and challenges of computational cost.

This research also performs a rapid DEM-based water mapping practice using the FwDET algorithm in the GEE platform. The mapping results and quality vary with the resolution of DEM, as demonstrated by the differences from each other in Figure 7. Generally, the higher the spatial resolution of the DEM data is, the better the details can be simulated by the FwDET, as in ALOS and SRTM results. All the DEM mapping results can detect flood inundation at low elevations. However, with the land use information missing, the urban drainage characteristics cannot be represented in such DEM products. The performance of the DEM-based model is limited due to lacking a representation of the hydrologic processes, including the infiltration and routing processes that could account for the overestimated water surfaces in areas A and C. Even with the fact that the DEM-based method is considered for urban pluvial flood mapping, urban drainage needs to be included for mapping such a case with this DEM approach. Nevertheless, the maps generated from DEM data can still help developing countries where credible flood hazard maps (e.g., U.S. FEMA flood layer) are unavailable.

To better leverage the application of the satellite-based water detection algorithms, it is suggested to perform localized sensitivity analysis to explore the validated threshold values (for both optical and SAR sensors), which will be used for rapid inundation identification in the high flood-risk area. It is also recommended to set up a standard workflow concerning water-related variables, data preprocessing, mapping algorithms, and validation metrics. Meanwhile, the DEM-based model can be improved by using high-resolution LiDAR DEM data as the input, in addition to considering the hydrologic and hydraulic processes of water routing, infiltration, and levee protection factors in the model. Land cover, land use, floodplain topography, and impervious surface percentage of the floodplain can be monitored and estimated using satellite observation and machine learning methods for up-to-date land surface monitoring to be further included in the DEM-based methods [65–68].

Finally, we would like to discuss the usage of flood detection provided by the aforementioned methods. These automated methods are rapid and can be easily applied for locations with limited resources, compared with other conventional and extensive hydrologic and hydraulic analyses. However, the advantage and disadvantages are somewhat obvious as well. Only a rough extent estimation can be provided that might lead to inefficient disaster management and rescue efforts, especially during a natural hazard. A more effective way to mitigate the impact of flood disasters is to incorporate a flood forecasting capability, such as flood early warning systems [69]. Later, in February 2022, Madagascar was struck by another cyclone, and the communities affected by those floods were left extremely vulnerable to any other hazards. While the flooding threat is already substantial, several ongoing trends, including rising precipitation intensity, could result in significant increases in flood risks in the near future. For a high-concentration climate change scenario, estimates from 11 climate models converge on the conclusion that flood frequencies in the high flood-risk regions for Southeast Asia, East and Central Africa, and large parts of Latin America could increase substantially in this century [1]. Undoubtfully, remote sensing data during or after the events can also be integrated into the flood models as validation data for rapid response evaluation and data assimilation processes in both physical and data-driven methods [70]. Above all, flood hazard maps [71], flood early warning systems, and satellite-derived flooding information from this research will be valuable to augment the comprehensive information available for stakeholders and communities to perform efficient flood management.

5. Conclusions

This study demonstrates delineated floodwater maps using optical and SAR imageries from the Landsat-7/8/9, Sentinel-2, and Sentinel-1 missions, respectively. Three popular automated algorithms, including Edge Otsu, Bmax Otsu, and Fuzzy Otsu, are compared for the 2022 Madagascar flooding event. All 30 m mNDWI maps produced by Edge Otsu, Bmax Otsu, and Fuzzy Otsu show more flooded areas of water bodies than those estimated from Sentinel-1 SAR imagery based on the same methods. Compared to Fuzzy Otsu, Edge Otsu and Bmax Otsu are more likely to generate similar results. The Fuzzy Otsu, as a more flexible method, needs additional model parameter settings that require more extensive tuning and calibration efforts to achieve desirable results.

In addition, a DEM-based tool (FwDET) uses six different DEM data sources for water extent estimation for the same event. DEM-based maps show general consistency with the reference map and satellite-based mapping results. This study showcases that developing countries such as Madagascar will benefit from some of the advanced surface water mapping products demonstrated in this study for better flood risk assessment in the future.

References

1. Hirabayashi, Y.; Mahendran, R.; Koirala, S.; Konoshima, L.; Yamazaki, D.; Watanabe, S.; Kim, H.; Kanae, S. Global Flood Risk under Climate Change. *Nat. Clim Chang.* **2013**, *3*, 816–821. [CrossRef]
2. Sharif, H.O.; Al-Juaidi, F.H.; Al-Othman, A.; Al-Dousary, I.; Fadda, E.; Jamal-Uddeen, S.; Elhassan, A. Flood Hazards in an Urbanizing Watershed in Riyadh, Saudi Arabia. *Geomat. Nat. Hazards Risk* **2016**, *7*, 702–720. [CrossRef]
3. Peng, B.; Huang, Q.; Vongkusolkit, J.; Gao, S.; Wright, D.B.; Fang, Z.N.; Qiang, Y. Urban Flood Mapping With Bitemporal Multispectral Imagery Via a Self-Supervised Learning Framework. *IEEE J. Sel. Top. Appl. Earth Obs. Remote Sens.* **2021**, *14*, 2001–2016. [CrossRef]
4. Fang, Z.; Dolan, G.; Sebastian, A.; Bedient, P.B. Case Study of Flood Mitigation and Hazard Management at the Texas Medical Center in the Wake of Tropical Storm Allison in 2001. *Nat. Hazards Rev.* **2014**, *15*, 05014001. [CrossRef]
5. Zhao, G.; Gao, H. Estimating Reservoir Evaporation Losses for the United States: Fusing Remote Sensing and Modeling Approaches. *Remote Sens. Environ.* **2019**, *226*, 109–124. [CrossRef]
6. Nguyen, P.; Thorstensen, A.; Sorooshian, S.; Hsu, K.; AghaKouchak, A. Flood Forecasting and Inundation Mapping Using HiResFlood-UCI and Near-Real-Time Satellite Precipitation Data: The 2008 Iowa Flood. *J. Hydrometeorol.* **2015**, *16*, 1171–1183. [CrossRef]
7. Munasinghe, D.; Cohen, S.; Huang, Y.-F.; Tsang, Y.-P.; Zhang, J.; Fang, Z. Intercomparison of Satellite Remote Sensing-Based Flood Inundation Mapping Techniques. *J. Am. Water Resour. Assoc.* **2018**, *54*, 834–846. [CrossRef]
8. Farhadi, H.; Najafzadeh, M. Flood Risk Mapping by Remote Sensing Data and Random Forest Technique. *Water* **2021**, *13*, 3115. [CrossRef]
9. Wouters, L.; Couasnon, A.; de Ruiter, M.C.; van den Homberg, M.J.; Teklesadik, A.; de Moel, H. Improving flood damage assessments in data-scarce areas by retrieval of building characteristics through UAV image segmentation and machine learning–a case study of the 2019 floods in southern Malawi. *Nat. Hazards Earth Syst. Sci.* **2012**, *21*, 3199–3218. [CrossRef]
10. Schroeder, R.; McDonald, K.; Chapman, B.; Jensen, K.; Podest, E.; Tessler, Z.; Bohn, T.; Zimmermann, R. Development and Evaluation of a Multi-Year Fractional Surface Water Data Set Derived from Active/Passive Microwave Remote Sensing Data. *Remote Sens.* **2015**, *7*, 16688–16732. [CrossRef]

11. Revilla-Romero, B.; Hirpa, F.; Pozo, J.; Salamon, P.; Brakenridge, R.; Pappenberger, F.; De Groeve, T. On the Use of Global Flood Forecasts and Satellite-Derived Inundation Maps for Flood Monitoring in Data-Sparse Regions. *Remote Sens.* **2015**, *7*, 15702–15728. [CrossRef]

12. Kansara, P.; Li, W.; El-Askary, H.; Lakshmi, V.; Piechota, T.; Struppa, D.; Abdelaty Sayed, M. An Assessment of the Filling Process of the Grand Ethiopian Renaissance Dam and Its Impact on the Downstream Countries. *Remote Sens.* **2021**, *13*, 711. [CrossRef]

13. Horritt, M.S. Calibration of a Two-Dimensional Finite Element Flood Flow Model Using Satellite Radar Imagery. *Water Resour. Res.* **2000**, *36*, 3279–3291. [CrossRef]

14. Bhattacharya, B.; Mazzoleni, M.; Ugay, R. Flood Inundation Mapping of the Sparsely Gauged Large-Scale Brahmaputra Basin Using Remote Sensing Products. *Remote Sens.* **2019**, *11*, 501. [CrossRef]

15. Massari, C.; Brocca, L.; Tarpanelli, A.; Moramarco, T. Data Assimilation of Satellite Soil Moisture into Rainfall-Runoff Modelling: A Complex Recipe? *Remote Sens.* **2015**, *7*, 11403–11433. [CrossRef]

16. Reager, J.; Thomas, A.; Sproles, E.; Rodell, M.; Beaudoing, H.; Li, B.; Famiglietti, J. Assimilation of GRACE Terrestrial Water Storage Observations into a Land Surface Model for the Assessment of Regional Flood Potential. *Remote Sens.* **2015**, *7*, 14663–14679. [CrossRef]

17. Fassoni-Andrade, A.C.; de Paiva, R.C.D.; Rudorff, C.d.M.; Barbosa, C.C.F.; Novo, E.M.L.d.M. High-Resolution Mapping of Floodplain Topography from Space: A Case Study in the Amazon. *Remote Sens. Environ.* **2020**, *251*, 112065. [CrossRef]

18. Shastry, A.; Durand, M. Water Surface Elevation Constraints in a Data Assimilation Scheme to Infer Floodplain Topography: A Case Study in the Logone Floodplain. *Geophys. Res. Lett.* **2020**, *47*, e2020GL088759. [CrossRef]

19. Feyisa, G.L.; Meilby, H.; Fensholt, R.; Proud, S.R. Automated Water Extraction Index: A New Technique for Surface Water Mapping Using Landsat Imagery. *Remote Sens. Environ.* **2014**, *140*, 23–35. [CrossRef]

20. Baig, M.H.A.; Zhang, L.; Shuai, T.; Tong, Q. Derivation of a Tasselled Cap Transformation Based on Landsat 8 At-Satellite Reflectance. *Remote Sens. Lett.* **2014**, *5*, 423–431. [CrossRef]

21. Lacaux, J.P.; Tourre, Y.M.; Vignolles, C.; Ndione, J.A.; Lafaye, M. Classification of Ponds from High-Spatial Resolution Remote Sensing: Application to Rift Valley Fever Epidemics in Senegal. *Remote Sens. Environ.* **2007**, *106*, 66–74. [CrossRef]

22. Kaptué, A.T.; Hanan, N.P.; Prihodko, L. Characterization of the Spatial and Temporal Variability of Surface Water in the Soudan-Sahel Region of Africa: SAHEL AND SOUDANIAN SURFACE WATER BODIES. *J. Geophys. Res. Biogeosci.* **2013**, *118*, 1472–1483. [CrossRef]

23. Halabisky, M.; Moskal, L.M.; Gillespie, A.; Hannam, M. Reconstructing Semi-Arid Wetland Surface Water Dynamics through Spectral Mixture Analysis of a Time Series of Landsat Satellite Images (1984–2011). *Remote Sens. Environ.* **2016**, *177*, 171–183. [CrossRef]

24. Huang, C.; Chen, Y.; Zhang, S.; Li, L.; Shi, K.; Liu, R. Spatial Downscaling of Suomi NPP–VIIRS Image for Lake Mapping. *Water* **2017**, *9*, 834. [CrossRef]

25. Isikdogan, F.; Bovik, A.C.; Passalacqua, P. Surface Water Mapping by Deep Learning. *IEEE J. Sel. Top. Appl. Earth Obs. Remote Sens.* **2017**, *10*, 4909–4918. [CrossRef]

26. Acharya, T.D.; Subedi, A.; Lee, D.H. Evaluation of Machine Learning Algorithms for Surface Water Extraction in a Landsat 8 Scene of Nepal. *Sensors* **2019**, *19*, 2769. [CrossRef]

27. DeVries, B.; Huang, C.; Lang, M.; Jones, J.; Huang, W.; Creed, I.; Carroll, M. Automated Quantification of Surface Water Inundation in Wetlands Using Optical Satellite Imagery. *Remote Sens.* **2017**, *9*, 807. [CrossRef]

28. Huang, W.; DeVries, B.; Huang, C.; Lang, M.; Jones, J.; Creed, I.; Carroll, M. Automated Extraction of Surface Water Extent from Sentinel-1 Data. *Remote Sens.* **2018**, *10*, 797. [CrossRef]

29. Kordelas, G.; Manakos, I.; Aragonés, D.; Díaz-Delgado, R.; Bustamante, J. Fast and Automatic Data-Driven Thresholding for Inundation Mapping with Sentinel-2 Data. *Remote Sens.* **2018**, *10*, 910. [CrossRef]

30. Cao, H.; Zhang, H.; Wang, C.; Zhang, B. Operational Flood Detection Using Sentinel-1 SAR Data over Large Areas. *Water* **2019**, *11*, 786. [CrossRef]

31. Donchyts, G.; Schellekens, J.; Winsemius, H.; Eisemann, E.; van de Giesen, N. A 30 m Resolution Surface Water Mask Including Estimation of Positional and Thematic Differences Using Landsat 8, SRTM and OpenStreetMap: A Case Study in the Murray-Darling Basin, Australia. *Remote Sens.* **2016**, *8*, 386. [CrossRef]

32. Bazi, Y.; Melgani, F.; Bruzzone, L.; Vernazza, G. A Genetic Expectation-Maximization Method for Unsupervised Change Detection in Multitemporal SAR Imagery. *Int. J. Remote Sens.* **2009**, *30*, 6591–6610. [CrossRef]

33. Dempster, A.P.; Laird, N.M.; Rubin, D.B. Maximum Likelihood from Incomplete Data Via the *EM* Algorithm. *J. R. Stat. Soc. Ser. B Methodol.* **1977**, *39*, 1–22. [CrossRef]

34. Gstaiger, V.; Huth, J.; Gebhardt, S.; Wehrmann, T.; Kuenzer, C. Multi-Sensoral and Automated Derivation of Inundated Areas Using TerraSAR-X and ENVISAT ASAR Data. *Int. J. Remote Sens.* **2012**, *33*, 7291–7304. [CrossRef]

35. Kuenzer, C.; Guo, H.; Schlegel, I.; Tuan, V.; Li, X.; Dech, S. Varying Scale and Capability of Envisat ASAR-WSM, TerraSAR-X Scansar and TerraSAR-X Stripmap Data to Assess Urban Flood Situations: A Case Study of the Mekong Delta in Can Tho Province. *Remote Sens.* **2013**, *5*, 5122–5142. [CrossRef]

36. Bioresita, F.; Puissant, A.; Stumpf, A.; Malet, J.-P. A Method for Automatic and Rapid Mapping of Water Surfaces from Sentinel-1 Imagery. *Remote Sens.* **2018**, *10*, 217. [CrossRef]

37. Liang, J.; Liu, D. A Local Thresholding Approach to Flood Water Delineation Using Sentinel-1 SAR Imagery. *ISPRS J. Photogramm. Remote Sens.* **2020**, *159*, 53–62. [CrossRef]

38. Chen, S.; Huang, W.; Chen, Y.; Feng, M. An Adaptive Thresholding Approach toward Rapid Flood Coverage Extraction from Sentinel-1 SAR Imagery. *Remote Sens.* **2021**, *13*, 4899. [CrossRef]

39. Jafarzadegan, K.; Muñoz, D.F.; Moftakhari, H.; Gutenson, J.L.; Savant, G.; Moradkhani, H. Real-Time Coastal Flood Hazard Assessment Using DEM-Based Hydrogeomorphic Classifiers. *Nat. Hazards Earth Syst. Sci.* **2022**, *22*, 1419–1435. [CrossRef]

40. Cohen, S.; Brakenridge, G.R.; Kettner, A.; Bates, B.; Nelson, J.; McDonald, R.; Huang, Y.; Munasinghe, D.; Zhang, J. Estimating Floodwater Depths from Flood Inundation Maps and Topography. *J. Am. Water Resour. Assoc.* **2018**, *54*, 847–858. [CrossRef]

41. Gorelick, N.; Hancher, M.; Dixon, M.; Ilyushchenko, S.; Thau, D.; Moore, R. Google Earth Engine: Planetary-Scale Geospatial Analysis for Everyone. *Remote Sens. Environ.* **2017**, *202*, 18–27. [CrossRef]

42. World Bank Climate Change Knowledge Portal. Available online: https://climateknowledgeportal.worldbank.org/ (accessed on 27 July 2022).

43. Randriamarolaza, L.Y.A.; Aguilar, E.; Skrynyk, O.; Vicente-Serrano, S.M.; Domínguez-Castro, F. Indices for Daily Temperature and Precipitation in Madagascar, Based on Quality-controlled and Homogenized Data, 1950–2018. *Int. J. Climatol.* **2022**, *42*, 265–288. [CrossRef]

44. Madagascar: Deadly Tropical Storms Cause Flooding, Landslides. Available online: https://news.un.org/en/story/2022/01/1110532 (accessed on 22 July 2022).

45. Huffman, G.J.; Stocker, E.F.; Bolvin, D.T.; Nelkin, E.J.; Tan, J. GPM IMERG Final Precipitation L3 1 month 0.1 degree x 0.1 degree V06, Greenbelt, MD, Goddard Earth Sciences Data and Information Services Center (GES DISC). 2019. Available online: https://disc.gsfc.nasa.gov/datasets/GPM_3IMERGDF_06/summary (accessed on 1 May 2022).

46. Xu, H. Modification of Normalised Difference Water Index (NDWI) to Enhance Open Water Features in Remotely Sensed Imagery. *Int. J. Remote Sens.* **2006**, *27*, 3025–3033. [CrossRef]

47. Twele, A.; Cao, W.; Plank, S.; Martinis, S. Sentinel-1-Based Flood Mapping: A Fully Automated Processing Chain. *Int. J. Remote Sens.* **2016**, *37*, 2990–3004. [CrossRef]

48. Markert, K.N.; Markert, A.M.; Mayer, T.; Nauman, C.; Haag, A.; Poortinga, A.; Bhandari, B.; Thwal, N.S.; Kunlamai, T.; Chishtie, F.; et al. Comparing Sentinel-1 Surface Water Mapping Algorithms and Radiometric Terrain Correction Processing in Southeast Asia Utilizing Google Earth Engine. *Remote Sens.* **2020**, *12*, 2469. [CrossRef]

49. Tadono, T.; Ishida, H.; Oda, F.; Naito, S.; Minakawa, K.; Iwamoto, H. Precise Global DEM Generation by ALOS PRISM. *ISPRS Ann. Photogramm. Remote Sens. Spat. Inf. Sci.* **2014**, *2*, 71. [CrossRef]

50. Lehner, B.; Verdin, K.; Jarvis, A. New Global Hydrography Derived From Spaceborne Elevation Data. *Eos Trans. AGU* **2008**, *89*, 93. [CrossRef]

51. Yamazaki, D.; Ikeshima, D.; Tawatari, R.; Yamaguchi, T.; O'Loughlin, F.; Neal, J.C.; Sampson, C.C.; Kanae, S.; Bates, P.D. A High-Accuracy Map of Global Terrain Elevations: Accurate Global Terrain Elevation Map. *Geophys. Res. Lett.* **2017**, *44*, 5844–5853. [CrossRef]

52. Danielson, J.J.; Gesch, D.B. *Global Multi-Resolution Terrain Elevation Data 2010 (GMTED2010)*; US Department of the Interior, US Geological Survey: Washington, DC, USA, 2011.

53. Farr, T.G.; Rosen, P.A.; Caro, E.; Crippen, R.; Duren, R.; Hensley, S.; Kobrick, M.; Paller, M.; Rodriguez, E.; Roth, L.; et al. The Shuttle Radar Topography Mission. *Rev. Geophys.* **2007**, *45*, RG2004. [CrossRef]

54. Foga, S.; Scaramuzza, P.L.; Guo, S.; Zhu, Z.; Dilley, R.D.; Beckmann, T.; Schmidt, G.L.; Dwyer, J.L.; Joseph Hughes, M.; Laue, B. Cloud Detection Algorithm Comparison and Validation for Operational Landsat Data Products. *Remote Sens. Environ.* **2017**, *194*, 379–390. [CrossRef]

55. Jong-Sen, L.; Jen-Hung, W.; Ainsworth, T.L.; Kun-Shan, C.; Chen, A.J. Improved Sigma Filter for Speckle Filtering of SAR Imagery. *IEEE Trans. Geosci. Remote Sens.* **2009**, *47*, 202–213. [CrossRef]

56. Beauchemin, M.; Thomson, K.P.B.; Edwards, G. Optimization of the Gamma-Gamma MAP Filter for SAR Image Clutters. *Int. J. Remote Sens.* **1996**, *17*, 1063–1067. [CrossRef]

57. Lee, J.-S. Refined Filtering of Image Noise Using Local Statistics. *Comput. Graph. Image Process.* **1981**, *15*, 380–389. [CrossRef]

58. Vollrath, A.; Mullissa, A.; Reiche, J. Angular-Based Radiometric Slope Correction for Sentinel-1 on Google Earth Engine. *Remote Sens.* **2020**, *12*, 1867. [CrossRef]

59. Otsu, N. A Threshold Selection Method from Gray-Level Histograms. *IEEE Trans. Syst. Man Cybern.* **1979**, *9*, 62–66. [CrossRef]

60. Rambabu, P.; Raju, C.N. The Optimal Thresholding Technique for Image Segmentaion Using Fuzzy Otsu Method. *IJ-AI* **2015**, *4*, 81. [CrossRef]

61. Canny, J. A Computational Approach to Edge Detection. *IEEE Trans. Pattern Anal. Mach. Intell.* **1986**, *PAMI-8*, 679–698. [CrossRef]

62. Fuzzy Membership (Spatial Analyst)—ArcGIS Pro | Documentation. Available online: https://pro.arcgis.com/en/pro-app/2.8/tool-reference/spatial-analyst/fuzzy-membership.htm (accessed on 22 July 2022).

63. Cohen, S.; Raney, A.; Munasinghe, D.; Loftis, J.D.; Molthan, A.; Bell, J.; Rogers, L.; Galantowicz, J.; Brakenridge, G.R.; Kettner, A.J.; et al. The Floodwater Depth Estimation Tool (FwDET v2.0) for Improved Remote Sensing Analysis of Coastal Flooding. *Nat. Hazards Earth Syst. Sci.* **2019**, *19*, 2053–2065. [CrossRef]

64.   Peter, B.G.; Cohen, S.; Lucey, R.; Munasinghe, D.; Raney, A.; Brakenridge, G.R. Google Earth Engine Implementation of the Floodwater Depth Estimation Tool (FwDET-GEE) for Rapid and Large Scale Flood Analysis. *IEEE Geosci. Remote Sens. Lett.* **2022**, *19*, 1–5. [CrossRef]
65.   Li, W.; El-Askary, H.; Lakshmi, V.; Piechota, T.; Struppa, D. Earth Observation and Cloud Computing in Support of Two Sustainable Development Goals for the River Nile Watershed Countries. *Remote Sens.* **2020**, *12*, 1391. [CrossRef]
66.   Brown, C.F.; Brumby, S.P.; Guzder-Williams, B.; Birch, T.; Hyde, S.B.; Mazzariello, J.; Czerwinski, W.; Pasquarella, V.J.; Haertel, R.; Ilyushchenko, S.; et al. Dynamic World, Near Real-Time Global 10 m Land Use Land Cover Mapping. *Sci. Data* **2022**, *9*, 251. [CrossRef]
67.   El-Askary, H.; Fawzy, A.; Thomas, R.; Li, W.; LaHaye, N.; Linstead, E.; Piechota, T.; Struppa, D.; Sayed, M.A. Assessing the Vertical Displacement of the Grand Ethiopian Renaissance Dam during Its Filling Using DInSAR Technology and Its Potential Acute Consequences on the Downstream Countries. *Remote Sens.* **2021**, *13*, 4287. [CrossRef]
68.   Braun, A. Retrieval of Digital Elevation Models from Sentinel-1 Radar Data—Open Applications, Techniques, and Limitations. *Open Geosci.* **2021**, *13*, 532–569. [CrossRef]
69.   Li, D.; Fang, Z.N.; Bedient, P.B. Flood Early Warning Systems under Changing Climate and Extreme Events. In *Climate Change and Extreme Events*; Elsevier: Amsterdam, The Netherlands, 2021; pp. 83–103. ISBN 978-0-12-822700-8.
70.   Sanders, W.; Li, D.; Li, W.; Fang, Z.N. Data-Driven Flood Alert System (FAS) Using Extreme Gradient Boosting (XGBoost) to Forecast Flood Stages. *Water* **2022**, *14*, 747. [CrossRef]
71.   Fang, Z.; Bedient, P.B.; Benavides, J.; Zimmer, A.L. Enhanced Radar-Based Flood Alert System and Floodplain Map Library. *J. Hydrol. Eng.* **2008**, *13*, 926–938. [CrossRef]